THE JOURNAL OF PHYSICAL CHEMISTRY C
A JOURNAL OF THE AMERICAN CHEMICAL SOCIETY

pubs.acs.org/JPCC Article

Thermal Transport in Engineered Hybrid Organic–Inorganic Perovskite Metasurfaces

Saswata Halder,* Amit Kessel, Noa Mazurski, and Uriel Levy*

Cite This: https://doi.org/10.1021/acs.jpcc.0c10187 Read Online

ABSTRACT: Halide perovskites have recently gained widespread attention for their exceptional optoelectronic properties, which have been illuminated by extensive spectroscopic investigations. In this study, nanophotonic surface engineering using a newly developed soft lithographic technique has been used to reproduce nanostructures with enhanced optical functionalities. The thermal sensitivity of the metasurfaces is first observed in the temperature-dependent photoluminescence (PL) spectra. In order to observe the local changes in heat transport induced by nanopatterning of the perovskite thin films, a noninvasive optical technique based on Raman spectroscopy is employed. The thermophysical properties of the engineered perovskite surfaces are extracted from the softening of the representative peak positions in the Raman spectra, which act as temperature markers. The investigation suggests a comparatively higher rise in the local temperature for the patterned thin films as compared to the pristine thin films. We characterize different imprint geometries on perovskite thin films in terms of both optical and thermal transport simultaneously and report for the first time the existence of a window of thermal tolerance for the metasurfaces within which optical efficiencies can still be maximized.

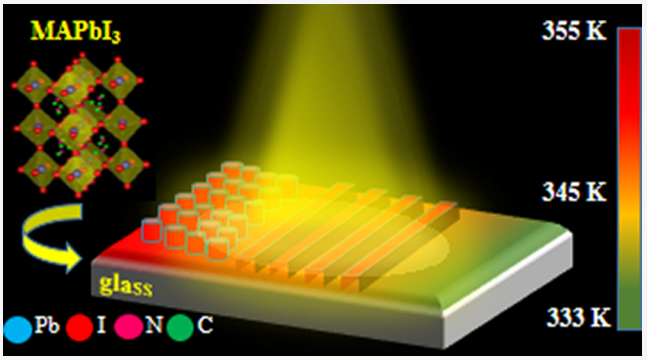

1. INTRODUCTION

The hybrid organic–inorganic halide perovskite $CH_3NH_3PbI_3$ (MAPbI) with an ABX_3 architecture has recently been demonstrated as a successful optical and optoelectronic material owing to its tunable direct band gap, long carrier lifetimes, high carrier mobilities, and diffusion lengths.[1−3] In addition, the low cost and facile fabrication of MAPbI thin films in solution form are advantageous in terms of their large-scale industrial preparation.[4,5] The nanopatterning of perovskite thin films has been shown to improve the efficiency of solar cells through reduced surface reflectance, tailored light trapping, and higher external radiative efficiency and directionality.[6−8] Researchers have demonstrated different techniques for the fabrication of perovskite metasurfaces ranging from etching of the substrate and subsequent conformal coating to direct patterning using focused ion beam milling.[9−13] Soft polymer-based imprinting techniques are appropriate for halide perovskites due to their sensitivity to water and plasma processing present in conventional lithography and etching processes. This goal was achieved by employing nanoimprint lithography using an inflexible stamp (silicon, Si) as well as using more flexible polydimethylsiloxane (PDMS) stamps.[14−19] Unlike an inflexible Si stamp, PDMS can imprint its textures conformally over nonuniform surfaces and defects.[20] The process also proves to be cost-effective as multiple PDMS stamps could be recycled from a single master.

MAPbI perovskites have been known to degrade upon prolonged exposure to heat and light since it is hard to avoid temperature increase and light soaking for solar cells/LEDs during their operation.[21−25] One of the contributing factors for the heat sensitivity of the perovskites is their ultralow thermal conductivity (0.2−0.5 WK^{-1} m^{-1}), which is a result of both the coupling of the MA cations to the inorganic PbI_2 cage and an overall tetragonal-to-cubic phase transition.[26−31] Raman and photoluminescence (PL) spectroscopies are widely used nondestructive noncontact methods to demonstrate the thermal transport in materials.[32−34] The laser beam serves a dual purpose: (i) a source of photons, which get scattered inelastically by the material, and (ii) a heat source, which increases the local temperature of the material at the point of incidence. The increase in the local temperature depends on the phonon transport; therefore, temperature- and excitation power-dependent optical measurements enable us to map the lattice vibrations of the materials to their thermal properties. The Raman spectra of MAPbI perovskites have been studied in

Received: November 11, 2020
Revised: June 7, 2021

https://doi.org/10.1021/acs.jpcc.0c10187
J. Phys. Chem. C XXXX, XXX, XXX−XXX

detail by many researchers.[35−41] The MAPbI structure features a significant dynamical disorder, which is aptly visualized through lattice vibrations (phonons) and molecular rotations.[42−44] Although electron−phonon interactions have a substantial influence on the solar cell operations, phonon−phonon scattering is directly related to the thermal properties of the perovskite.[45−47] The low thermal conductivity in perovskites is directly related to the phonon lifetimes. The phonon lifetime is essential as it provides critical insights into the different electron−phonon and phonon−phonon couplings occurring in the material.[48] The hybrid organic−inorganic lattice in MAPbI has larger lattice parameters than fully inorganic counterparts. The incoherent rattling motion of the MA atoms embedded in the PbI_2 cage, coupled with the Pb−I vibrations, provides the requisite phonon scattering. The ultralow thermal conductivity of the MAPbI (∼0.18 W/$K^{-1}m^{-1}$) material is intrinsically due to the large cations in the Pb−I inorganic cage and the weaker bonds, analogous to the case of PbI_2 with an already low thermal conductivity (∼0.32 W/$K^{-1}m^{-1}$).[49] Hata et al. showed that this further suppression of the thermal conductivity in MAPbI (∼0.18 W/$K^{-1}m^{-1}$) with respect to PbI_2 (∼0.32 W/$K^{-1}m^{-1}$) results from the introduction of MA cations in the soft inorganic lattice and the corresponding coupling of the librational modes to Pb−I vibrations.[50] Indeed, this suppression mechanism of the MA cation on the lattice thermal conductivity was demonstrated using ab initio molecular dynamics (AIMD) simulations with different crystal structure models, which included and excluded the MA cation from the inorganic cage of PbI_2, respectively. The results claimed that the thermal transport is mainly suppressed by a complicated dynamical switching between the translation and rotational motions of the MA cations, which are then coupled to the low-frequency Pb−I vibrations.[50] AIMD simulations along with the third-order perturbation theory have predicted very short phonon lifetimes of ∼20 and ∼1 ps at the Brillouin zone center and Brillouin zone boundaries, respectively, for such low-frequency modes (∼14 cm^{-1}).[51−54] The short phonon lifetimes mean that the phonons do not efficiently dissipate heat and can therefore affect the carrier relaxation and phonon−phonon scattering processes. The inefficient dissipation of heat can result in a localized increase in temperature accelerating the destabilization process for the halide perovskites. Within the realms of our experimental setup, the modes mostly affected by changes in temperature are the MA ion librational mode at 110 cm^{-1} and the Pb−I stretching mode at 96 cm^{-1}. In the spectral range of investigation, the highest vibrational peak with a profound temperature dependence occurs at 110 cm^{-1} and thus is considered for the present study for Raman thermometry. The mode at 96 cm^{-1} effectively behaves as quasi-harmonic and is therefore not considered for the present study. We extract the thermal variation of the detected Raman peaks to intuitively understand the temperature-dependent phonon process.

In this study, we make use of the conventional Raman and PL spectroscopy techniques to demonstrate the optical and thermal transport mechanisms in surface-patterned MAPbI perovskite thin films. We adopt a surface imprinting method coherent with a thin spin-coated precursor MAPbI perovskite film in a soft gel state imprinted with a topographically prepatterned elastomeric PDMS mold.[55] Temperature-dependent PL measurements are conducted to demonstrate the temperature sensitivity of the emission properties in the nanostructured thin films. The analysis of the Raman active modes as a function of temperature and laser power for both the prepatterned and patterned perovskites is performed to extract a quantitative change in the local thermal behavior. The study concludes with a discussion of the thermal transport mechanism in planar and patterned perovskite films with possible consequences on the working efficiency of a solar cell/optical device, elucidating the requirement of defining a workable thermal window for spatially patterned MAPbI thin films.

2. EXPERIMENTAL DETAILS

2.1. Synthesis of the MAPbI Perovskite Solution. Initial ingredients of methylammonium iodide (MAI, 99.99%, Ossila) and lead iodide (PbI_2, 99.99%, Sigma-Aldrich) were taken in accordance with the stoichiometric ratio. A solution of *N*,*N*-dimethylformamide (DMF, 99.99%, Sigma-Aldrich) and dimethyl sulfoxide (DMSO, 99.99%, Sigma-Aldrich) was prepared in a molar ratio of 4:1. A stoichiometric powder mixture of MAI (0.159 g) and PbI_2 (0.461 g) was dissolved in the DMF:DMSO solution to prepare a 1 M solution (1 mL) inside a nitrogen-filled glove box. The solution was kept at 60 °C on a hot plate with constant magnetic stirring for 3−5 h for homogeneous mixing of the powder in the solution.

2.2. Preparation of PDMS Stamp. A Si chip (20 mm × 20 mm) was cleaned with "Piranha" (H_2SO_4:H_2O_2, 3:1). Two surface imprints of interest were prepared for the present study: (i) a grating with width = 1.3 μm, period = 2.6 μm, and height = 150 nm and (ii) an array of nanosphere with a radius of 225 nm. The pattern was subjected to spin coating of an electron beam resist (ZEP 520A) followed by electron beam lithography (ELS-G100 Elionix). The pattern was transferred to the Si chip by reactive ion etching (Corial 200I) with a mixture of SF_6 and CHF_3. After etching, the remaining ZEP was stripped and the sample was cleaned with "Piranha." A layer of octadecyltrichlorosilane was formed on the Si master surface to make the Si substrate hydrophobic. Gelest h-PDMS base and curing agents were mixed in a ratio of 1:1. The mixture was degassed for a few minutes until all the air bubbles disappeared. The h-PDMS was spin coated on the precleaned Si master for 30 s at 2000 revolutions per minute (RPM). The spin-coated complex was degassed again to remove any residual air bubbles. The h-PDMS−Si substrate was then partially cured in the oven for 30 min at 65 °C until h-PDMS was slightly sticky. SYLGARD 184 base and curing agents were mixed in a ratio of 5:1. The mixture was degassed until all the air bubbles disappeared. s-PDMS was poured on top of the h-PDMS layer and degassed for about 1 h and subsequently cured at 65 °C for 12 h. The h-PDMS/s-PDMS stamp was then gently detached from the Si master.

2.3. Fabrication of Patterned Thin Films. Glass substrates having dimensions of 15 mm × 20 mm were cleaned by ultrasonication successively in deionized water, acetone, and isopropyl alcohol and dried with nitrogen gas. They were then further cleaned in an O_2 plasma atmosphere for 10 min to make the surface hydrophilic for uniform wetting of the substrates with the perovskite precursor solution. The cleaned substrates were transferred inside the glove box and spin coated with the perovskite precursor solution in a two-step process initially at 1000 RPM for 10 s followed by 3000 RPM for 20 s. During the spin-coating process, toluene solution (15−20 μL) was added dropwise to the precursor solution. This antisolvent treatment prevents unwanted nucleation of the perovskite solution during spin coating,

https://doi.org/10.1021/acs.jpcc.0c10187
J. Phys. Chem. C XXXX, XXX, XXX−XXX

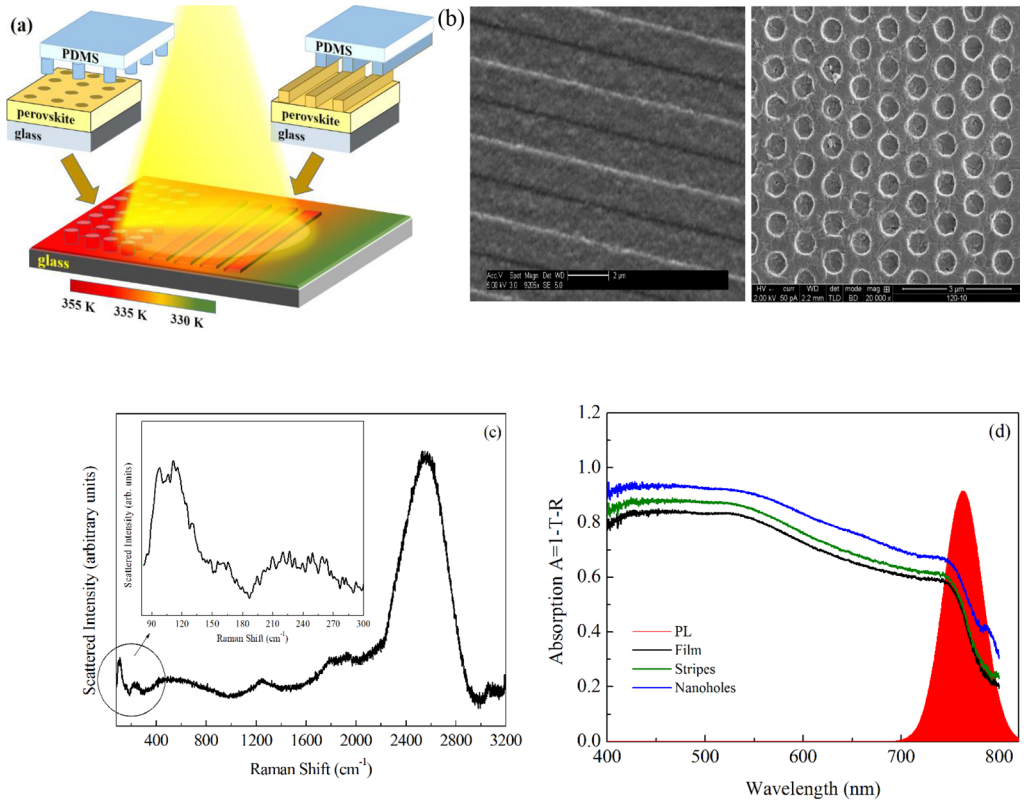

Figure 1. (a) Schematic representation of surface-patterned perovskites and their corresponding properties. (b) SEM images of MAPbI stripes and nanoholes. (c) Raman spectra of MAPbI. The inset shows the region of interest for the present study. (d) Absorption and PL spectra of MAPbI pristine, stripes, and nanoholes.

resulting in improved crystallization.[56] For the patterned films, elastomeric PDMS stamp, with the designated patterns, was placed face down on the spin-coated gel and annealed at 90 °C under an applied pressure of 4 kgcm^{-2} for 15 min for the final crystallization and the removal of excess solvent.

2.4. Characterization. The X-ray diffraction (XRD) spectra of the samples were measured using a Bruker D8 Advance X-ray diffractometer in the range of $10° < 2\theta < 80°$ using a step size of 0.01°. The scanning electron microscopy (SEM) images were obtained with an extra high-resolution scanning electron microscope Magellan TM 400 L. Transmission and reflection spectra were measured using a custom microscope setup. For transmission, the sample was illuminated with a white light source (tungsten-halogen lamp) using a microscope condenser lens. The transmitted light was collected by an objective lens (Nikon, 50×, NA 0.45) and taken to a fiber-coupled Ocean Optics Flame spectroscope. Reflection measurements were carried out in an inverted reflection microscope configuration using the same light source, objective lens, and spectrometer. The absorption was calculated from reflection and transmission using the relation $A = 1 - R - T$. The Raman and PL spectra for the samples were measured using a Renishaw inVia Raman spectrometer, which was equipped with a 2400 lines per mm grating and a Peltier-cooled CCD. A 50× objective was used to focus the laser beam on the sample with a spot diameter of ∼1 μm. For the temperature-dependent PL measurements, the sample was placed in a heating setup and the laser power was fixed to 20 μW to reduce any additional heating from the laser at the point of incidence. The Raman measurements were carried out under ambient conditions with an excitation wavelength of 514 nm with varying laser powers. The temperature at the measurement point was extracted using eq 1. The baseline-corrected Raman spectrum was deconvoluted with a Lorentzian lineshape, and the individual contributions of constituent peaks were obtained by refining the peak position, full width at half maximum (FWHM), and amplitude. The X-ray photoemission spectra of the samples were recorded using an X-ray photoelectron spectroscope (Axis Supra). X-ray photoelectron spectroscopy (XPS) profiles of the samples were acquired using a monochromatic Al Kα source with energy $h\nu$ = 1486.7 eV and operated at 15 kV and 15 mA. The binding energy was determined with reference to the C 1s line at 284.8 eV.

2.5. Numerical Simulations. Finite-difference time-domain (FDTD) simulations were performed using commercial software (Lumerical Inc., FDTD Solutions). The refractive index data used in the simulation were obtained from ref 57 after it was verified to produce similar results to the films.

3. RESULTS AND DISCUSSION

Figure 1a shows schematically the idea of probing a differential thermal transport mechanism simultaneously with a PL enhancement in textured perovskite films developed using the soft lithographic technique. The prepatterned and patterned perovskite thin films are characterized with the help of XRD as shown in Figure S1 of the Supporting Information. The difference in the quality of crystallization achieved is shown in Figure S1b,c for planar and imprinted films. The core-level XPS spectra for MAPbI (Figure S2, Supporting Information) show the characteristic signature peaks.[58] Figure 1b shows the SEM images of the stripe- and

https://doi.org/10.1021/acs.jpcc.0c10187
J. Phys. Chem. C XXXX, XXX, XXX−XXX

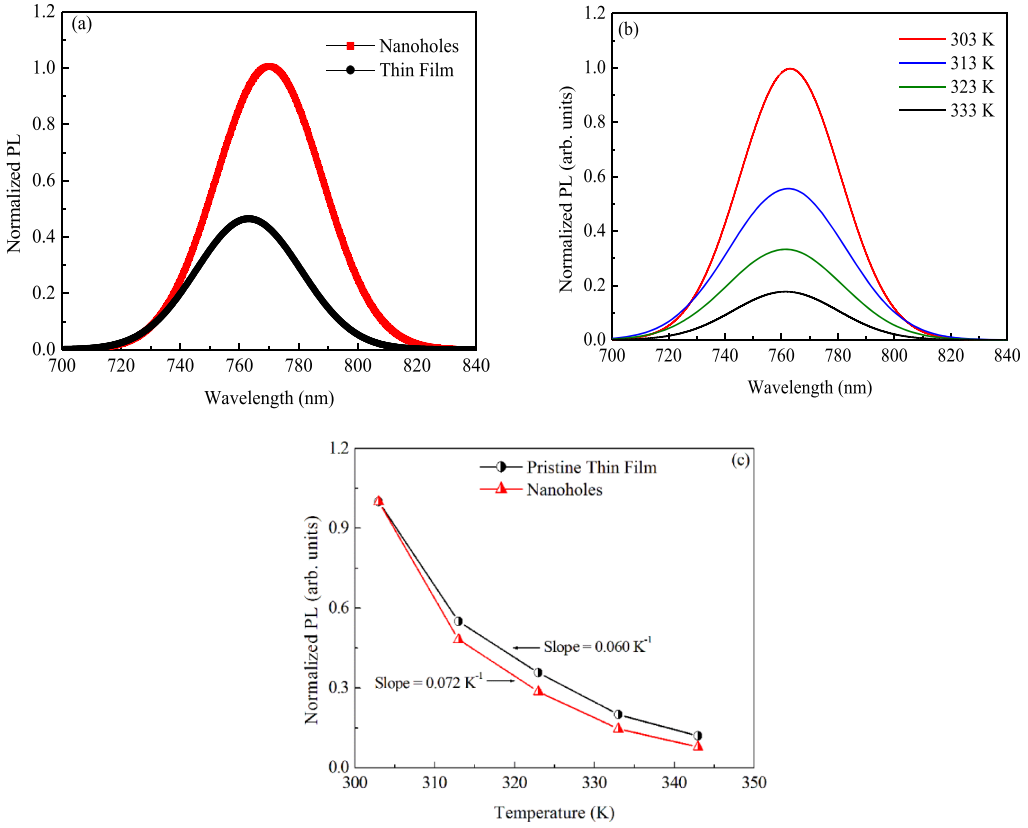

Figure 2. (a) PL spectra for MAPbI thin film and nanoholes, (b) temperature-dependent PL spectra for MAPbI planar thin film, and (c) variation of normalized PL intensity with temperature for both thin film and nanohole structures.

nanohole-patterned perovskite thin films, which are negative replications of the original PDMS mold. The height of the grating is 140 nm, with width and period of 1.3 and 2.6 μm, respectively. The average diameter of the nanohole is 493 nm, and the mean depth is 127 nm. These results demonstrate that although the perovskite is an ionic compound with no glass-transition behavior, it can still be imprinted using soft lithographic methods through molding into cavities under the application of heat and pressure. The use of the elastomeric stamp has a favorable crystallization effect on the thin film as it reduces regions of lower surface energy and prevents unwanted nucleation of the crystals forming isolated large arrays with pores (Figure S3, Supporting Information). Figure 1c shows the Raman spectra of a MAPbI film obtained under laser excitation of 514 nm with the inset defining the region of interest for our present study on Raman thermometry. Different sets of vibrational peaks are observed at low frequencies (80−250 cm^{-1}), mid frequencies (300−800 cm^{-1}), and higher frequencies (>800 cm^{-1}) having their origins due to the motion of the atoms inside the inorganic PbI_2 cage as well as the organic MA cations. The deconvoluted Raman spectra are shown in Figure S4a−c (Supporting Information), which show that an individual broad peak can be decoupled into smaller contributions. In Figure S4a, a Raman signal is observed between 80 and 170 cm^{-1} with peaks at 96, 110, and 126 cm^{-1}. The peak associated with 96 cm^{-1} is related to Pb−I stretching, whereas the region 100−200 cm^{-1} represents the librational motion of MA cations. The broad Raman band at 200−350 cm^{-1} is assigned to the torsional motion of the MA cations.[44] The range 400−3000 cm^{-1} (Figure S4b,c) is associated with the MA cations only and is independent of the vibrations of the inorganic component. These high-frequency vibrations are attributed to the bond stretching and angle deformation of MA cations. A detailed explanation of the origin of the vibrational modes in the Raman spectra of MAPbI is provided in Section S5 of the Supporting Information.

Optical characterizations were performed for the pristine and metasurface-designed thin films by measuring the reflection and transmission spectra across the visible regime averaged over several locations as shown in Figure 1d. MAPbI is very much absorptive to begin with and we observe an enhancement in absorption. Clearly, absorption enhancement will become more dominant for a thinner film device having a lower initial absorption. A clear resonance is not visible as the material is highly absorptive, which may dampen and broaden any existing resonant peak. Such resonances may significantly arise in the infrared regime, where the photon energies are below the band gap of MAPbI, and the structure loses its absorbing properties. The nanoholes show higher absorption than the planar films and stripes, ensuring higher photon absorption in the visible spectrum. We have not taken into account the surface scattering; so, we should note that the actual absorption will likely be slightly less than what is directly derived from the measurement. Since the planar films and nanoholes represent the two ends of the spectrum, to show this enhanced absorption, a FDTD simulation of the electric field in a nanohole array is performed and compared to the planar counterpart (Figure S9, Supporting Information). It confirms the presence of waveguide modes arising in the nanohole perovskite layer as well as an increased localization of the field inside the cavity. We observe that for longer wavelengths

https://doi.org/10.1021/acs.jpcc.0c10187
J. Phys. Chem. C XXXX, XXX, XXX−XXX

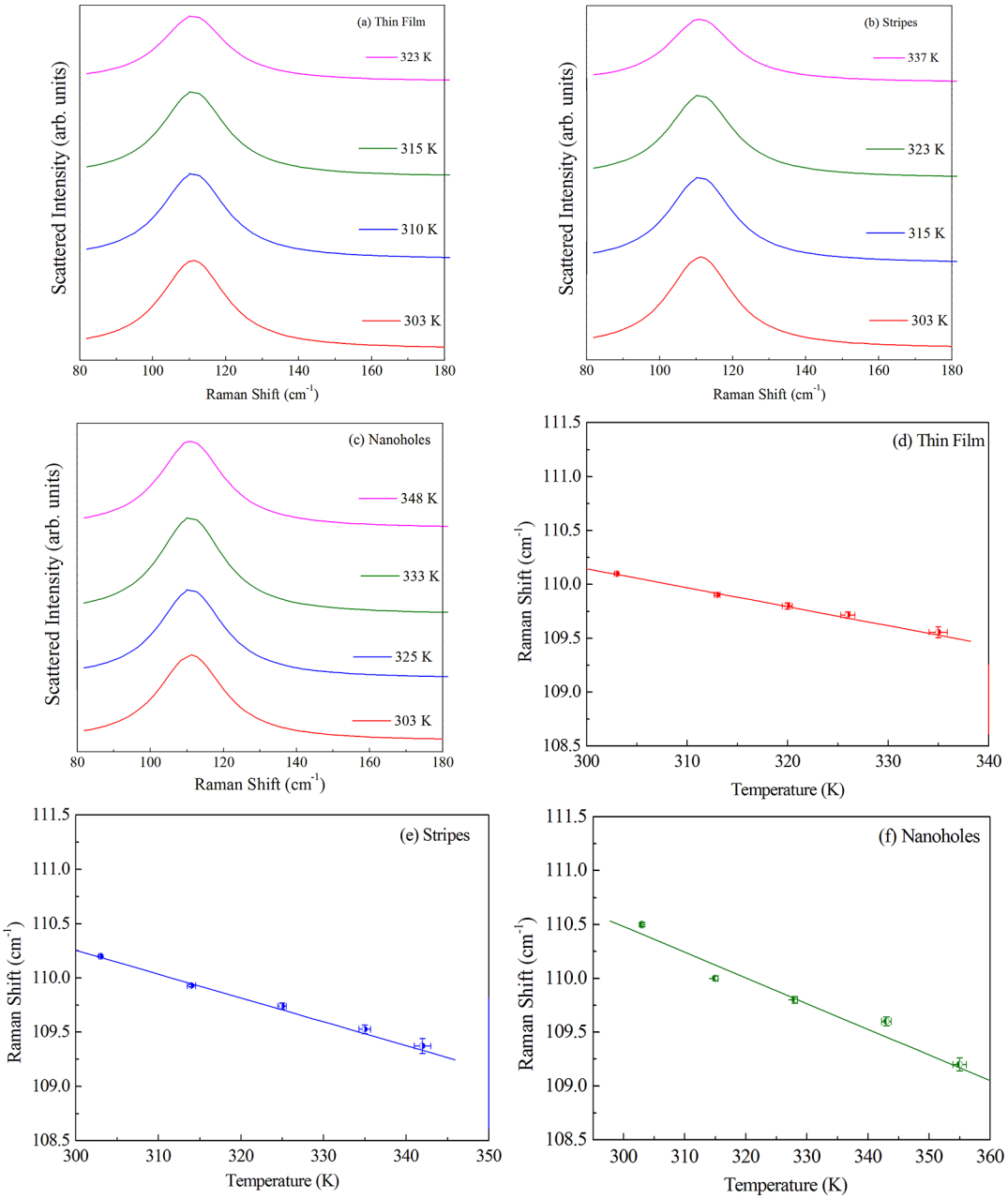

Figure 3. Temperature dependence of the deconvoluted Raman shift at 110 cm^{-1} for (a,d) thin film, (b,e) stripes, and (c,f) nanoholes. The temperature is extracted using eq 1.

(relative to the cavity size), the field is less localized in the cavity and leaks into the perovskite where it gets guided and absorbed. The absorption of the pristine and metasurfaces is calculated as $A = 1 - T - R$, where A is the absorption, R is the reflectance, and T is the transmittance. The metasurfaces exhibit strong light-trapping capabilities with enhanced absorption. In order to assess the contribution for generating free carriers under solar illumination, we calculated the portion of photons to be absorbed in the range of 400−800 nm under AM1.5 illumination by multiplying the absorption spectra with the irradiance from the Sun. For the planar film, we obtained an absorption of 69% of the photons, whereas for the nanohole metasurfaces, a value of 78% was found with the grating absorption showing an intermediate value. This corresponds to an overall 15% increase in the number of absorbed photons in the case of nanoholes.

MAPbI shows an efficient PL spectrum at 765 nm with a FWHM of 43 nm. The room temperature PL intensity of the nanoholes is higher than that of the thin film with a small redshift as shown in Figure 2a. To better understand the origin of the large PL enhancement, we consider the following plausible explanations. First, increased absorption will obviously contribute to external PL efficiency. However, we cannot singularly attribute the increased PL efficiency to enhanced absorption. The second most plausible explanation is the consideration of modified spontaneous emission arising from the photonic structure.[59] The emission rate of an emitter is dependent on the surrounding electromagnetic field and local photonic density of states.[60] Therefore, a stronger field confinement in the perovskite (Figure S9, Supporting Information) enhances the rate of emission. However, the most dominant contribution comes from the improved photon

https://doi.org/10.1021/acs.jpcc.0c10187
J. Phys. Chem. C XXXX, XXX, XXX−XXX

outcoupling in the thin film. It has already been established that photon recycling, the reabsorption of emitted photons, plays an important role in MAPbI,[61] which means that not all emitted photons exit the thin-film surface. The angle of incidence to the surface normal for a textured surface is relatively less compared to a planar film, which allows more photons to be outcoupled from the system and provides the necessary boost to the PL enhancement. The absorbed high-energy photons stimulate hot carriers in the perovskite with nonzero kinetic energy, which then decay to the band edge and transfer their kinetic energy to the lattice through phonon scattering, which when in thermal equilibrium result in heating the sample. Therefore, temperature-dependent PL spectroscopy can be used for investigating the heat sensitivity and heat fluctuations in samples, which can effectively act as markers for temperature sensitivity. The temperature-dependent PL spectra for the perovskite thin film show quenching on increased heating of the sample (Figure 2b). The dependency of normalized PL intensity on temperature is shown in Figure 2c. The PL of the nanoholes quenches faster with respect to the temperature than for the planar film.

The temperature-dependent PL spectra showed the enhanced thermal sensitivity of the nanostructures. In this section, we try and find an insight into the local thermal transport in perovskite thin-film metasurfaces. In order to investigate the thermal transport of the nanostructures, temperature- and laser power-dependent Raman spectra for the pristine and patterned perovskites are shown. Since temperature affects the density of iodine defects in perovskites, we identify that the modes mostly affected by changes in temperature are the MA ion librational mode and the Pb−I stretching mode at 110 and 96 cm^{-1}, respectively.[62] The 110 cm^{-1} branch is an in-plane vibration, whereas the 96 cm^{-1} branch represents an out-of-plane vibration of optical phonons. We consider the temperature dependence of both these vibrations for the present study.

The deconvoluted Raman profiles for the planar, striped, and nanohole perovskite systems in the range of 80−200 cm^{-1} for different laser excitations are shown in Figures S5−S7, respectively, in the Supporting Information. The laser acts as a localized heat source, and therefore, the Raman peak shifts act as appropriate temperature markers. The frequency shift due to phonon−phonon coupling is represented as[63,64]

$$\Delta\omega(T) = A\left[1 + \frac{2}{\exp\left(\frac{\hbar\omega_0}{2k_BT}\right) - 1}\right] + \omega_0[\exp(-3\gamma\beta T) - 1] \quad (1)$$

where ω_0 is the Raman frequency at 0 K, A is the anharmonic constant, γ is the Grüneisen parameter, and β is the coefficient of thermal expansion. The temperature at the measurement point is calculated from the variation of peak positions as a function of the incident laser power in accordance with eq 1. The deconvoluted Raman profiles at 110 cm^{-1} for the three samples at different temperatures are shown in Figure 3a−c, respectively. The Raman shift as a function of temperature for planar, stripe, and nanohole metasurfaces is shown in Figure 3d−f, respectively. The corresponding temperature dependence of the Raman shift at 96 cm^{-1} is shown in Figure S8 of the Supporting Information. The peak positions redshift with an increase in temperature, which indicates that the thermal properties of the samples are modified due to the heat from the laser.[63−65] In both the striped and nanohole perovskites, the temperature reaches around 343 and 355 K, respectively, compared to the planar film (∼335 K). A higher local rise in temperature is observed in patterned perovskites compared to the pristine sample. Considering a three-photon scattering process, the scattering mechanism is empirically defined as $\tau^{-1} = \tau_b^{-1} + \tau_p^{-1} + \tau_u^{-1}$,where τ_b^{-1} is due to the scattering from sample boundaries and τ_p^{-1} is due to scattering from point defects like vacancies, substitutions, and other pointlike impurities.[66] With the increase in temperature, phonon−phonon interactions start to dominate as given by the three-phonon Umklapp scattering $\tau_u^{-1} \propto T^3$.[66] τ_p^{-1} is mostly a bulk property of the sample and the effect of nanopatterning on it can be ignored as the patterning does not inherently change the vacancy defect densities in the materials. First, an increase in the absorption plays a role in increased energetic photon absorption. Due to the inherent ultralow thermal conductivity of the material, the spread of optically deposited heat will be hindered. Since the number of photoexcited carriers is low and their contribution to the thermal transport is negligible, the main contribution of the high-energy incident photons will be to heat the material.[67] Second, due to altered grain and grain boundary dimensions arising as an artifact of the patterning process, boundary scattering τ_b^{-1} also contributes to the thermal conductivity although its effect is much less than anticipated.[66,68] Therefore, the redshift in the phonon branches results from an increase in the phonon−phonon scattering (τ_u^{-1}). Thus, the phonon−phonon interactions in the nanopatterns may be more due to the increased rattling motion of the MA cations in the perovskite arising from the increased local heating of the sample.[69] It is worth noting that the contribution of the boundary scattering from the metasurfaces to the thermal transport is negligible.[66,68] In a way, the metasurfaces act as "localized heat concentrators," which concentrate the heat onto the perovskite underneath by absorbing high-energy photons. We quantify this heat sensitivity in the following section.

In order to understand quantitatively the heat sensitivity of the systems under investigation, we investigate the shift in phonon modes with respect to temperature. Figure 3d−f shows the Raman shift as a function of temperature due to laser-induced heating for planar and imprinted perovskite thin films. The Raman frequencies redshift with temperature, which can be analyzed by the following equation[34]

$$\omega(T) = \omega_0 + \chi_T T \quad (2)$$

where ω_0 is the phonon frequency at absolute zero and χ_T is the first-order temperature coefficient. By fitting the phonon redshift using eq 2, the obtained χ_T values for the pristine, grating, and nanohole perovskites are −0.018, −0.020, and −0.022 cm^{-1}/K, respectively. Recalling the thermal variation of the 96 cm^{-1} mode, we find that the corresponding χ_T values for pristine, grating, and nanohole perovskites are −0.008, −0.008, and −0.01 cm^{-1}/K, respectively. Apparently, the wavenumber decrease of in-plane phonons is much larger than that of the out-of-plane phonons, indicating a strong anisotropic temperature dependence of wavenumbers of phonons and consequently the thermal transport. This observation is similar to the case of layered PbI_2.[70] From the calculated values of χ_T, it is clear that the heat sensitivity of the nanoholes is more than those of the stripes and planar film, respectively. This is in direct correlation with the temperature-

https://doi.org/10.1021/acs.jpcc.0c10187
J. Phys. Chem. C XXXX, XXX, XXX−XXX

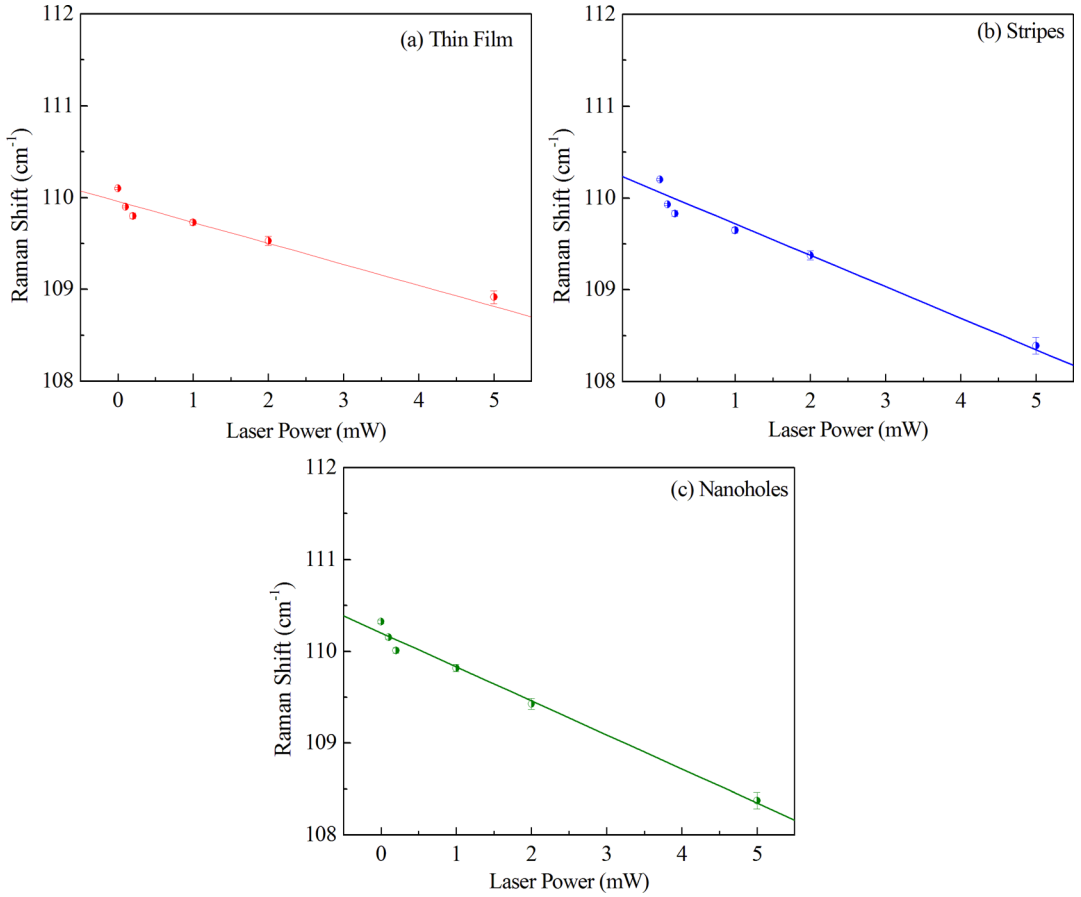

Figure 4. Raman shift of MAPbI thin films as a function of laser power for (a) thin film, (b) stripes, and (c) nanoholes.

dependent PL spectra for the thin film and nanohole perovskite, which present themselves as two extremes in the heat sensitivity spectrum.

The thermal transport, based on the observations of the temperature dependence of phonon wavenumbers, is anisotropic in nature. The in-plane thermal response far exceeds the out-of-plane thermal behavior. In order to quantify the change in the thermal transport upon optical irradiation, we try to estimate the change in the thermal conductivity based on our observations from Raman thermometry. The heat conduction through a surface with the cross-sectional area S can be evaluated from the equation: $\partial Q/\partial t = -K\oint(\nabla T.\mathrm{d}S)$ where Q is the amount of heat transferred over the time t and T is the absolute temperature. Considering a circular heat front propagating radially outward in a circular geometry, the thermal conductivity is given by $K = \gamma.(Q/\Delta T)$,[71] where $\gamma \propto 1/2\pi d$. Writing the uniform radial heat flow equation for the two laser excitation powers P_1 and P_2, corresponding to the two hot spot temperatures T_1 and T_2, respectively, the thermal conductivity is expressed as $K = (1/2\pi d)(\Delta P/\Delta T)$, where d is the thickness and the local temperature rise ΔT is due to the difference in the heating power $\Delta P = P_2 - P_1$. For low-excitation power levels, the peak position varies linearly with the sample temperature $\omega = \omega_0 + \chi_T T$. The final expression for the thermal conductivity in the radial heat wave case can be written as[72]

$$k = \chi_T\left(\frac{1}{2\pi d}\right)\left(\frac{\mathrm{d}\omega}{\mathrm{d}P}\right)^{-1} \quad (3)$$

where $\mathrm{d}\omega$ is a small shift in the peak position due to the variation $\mathrm{d}P$ in the heating power on the sample surface. Intuitively, a local temperature increase for two different materials will be lower for the material with higher thermal conductivity, assuming absorption to be constant. Considering the dominant in-plane response, the deconvoluted Raman shift as a function of laser power for the in-plane vibrations at 110 cm^{-1} obtained from Figures S5−S7 (Supporting Information) is shown in Figure 4a−c, respectively. We have estimated the slope $(\mathrm{d}\omega/\mathrm{d}P)$ from Figure 4a−c for the pristine, striped, and nanohole thin-film systems. Here, P represents the laser power. The solid lines are the linear fit to the experimental data. Shen et al. have shown that the thermal conductivity of MAPbI is independent of thickness (d) ranging between 90 and 400 nm.[71] Therefore, the effect of thickness "d" on the thermal conductivity (k) can be assumed to be negligible for all the three systems. Therefore, the only values of consideration are χ_T and $(\mathrm{d}\omega/\mathrm{d}P)$.

We categorize the three systems under investigation (pristine, striped, and nanoholes) as A, B, and C, respectively, with nearly equal absorption. The slope for the nanohole (−0.38 cm^{-1}/mW) is higher than the striped (−0.32 cm^{-1}/mW) and thin film (−0.27 cm^{-1}/mW) perovskites, respectively. The nanoholes show an ∼5% decrease in the in-plane thermal response with respect to the grating structure and an ∼11% decrease with respect to the planar film if the absorption in the samples is normalized with respect to the planar perovskite. Thus, the nanohole-MAPbI perovskite thin films act as material systems with reduced thermal conductivity compared to the grating-MAPbI and planar-MAPbI perovskite

https://doi.org/10.1021/acs.jpcc.0c10187
J. Phys. Chem. C XXXX, XXX, XXX−XXX

thin films. The inherent ultralow thermal conductivity of planar MAPbI hinders the distribution of the optically deposited heat. The reduced thermal conductivities in the grating and nanohole metasurface-MAPbI systems with respect to the planar film therefore mimic systems in which further restriction in the outward flow of heat is observed, giving rise to more local heating of the sample. These observations are therefore in direct correlation with the observations regarding the heat sensitivity, χ_T, and the PL quenching observed in Figure 2c. We propose that partial lithographic engineering of perovskite thin-film surfaces can therefore be an attractive way to set up thermal gradients required for developing thermal potentials. However, the effect of other factors like boundary scattering and grain boundary engineering need to be addressed to fully understand the mechanism of modulating thermal conductivity using perovskite metasurfaces. This work thus aims to offer an insight into designing future photothermal devices using perovskite metasurfaces. In a broader sense, this work for the first time also defines a window of thermal sensitivity for MAPbI thin film−metasurface systems in which we can maximize device functionalities for solar cells and other optical applications.

We now discuss the consequences of this increased thermal heating on optical/solar cell functioning. As mentioned earlier, nanoimprinting of perovskite thin films does not alter the defect density in the materials; the defect chemistry is solely dependent on the temperature. The defect states, which have significant impact on the optical degradation of the perovskite solar cells, are due to the migration of ions and their corresponding vacancies (quasi-ions). In order to understand how the enhanced absorption and the local heating may have a depressing effect on the working efficiency of the perovskite solar cells, we need to understand the temperature-dependent dynamics of the migrating ions in the material. There are two kinds of charge carriers that play a significant role in the working of solar cell/optical devices: (a) electrons and holes resulting from absorption are responsible for the power conversion process and (b) lattice defects in the form of ion vacancies caused by migrating ions result in the optical degradation of MAPbI.[73] Since the formation energy of MAPbI is very low, some amount of ionic and lattice defects exists in the materials at room temperature. These vacancies become ionized and take the form of quasi-ions when the material absorbs photons resulting in the formation of electron−hole pairs. Under the influence of the built-in electric field, the quasi-ions move toward the end of the perovskite layers giving rise to a reverse field. Thus with sufficient time, density of such quasi-ions increases and the working potential difference of the perovskite will be completely nullified and the charge carrier separation will cease.[74] These quasi-ions, which are responsible for additional energy levels below the conduction band minimum, will result in higher nonradiative recombination and therefore the PL will show quenching. Temperature can accelerate the change in the densities of defects and their migration toward the edges of the perovskite layers. For a 300−350 nm perovskite layer, the formation energies of iodine and MA vacancies are 0.41 and 0.49 eV, respectively, which are quite low and can be easily overcome with an increase in temperature.[75] Thus with the increase in temperature, the vibrational energy of ions in lattice structures also increases, which enhances the probability of an ion moving to the crystal surface, grain boundaries, or dislocation surfaces. It has been shown experimentally that with an increase in temperature, the number of ions inside the layer volume decreases and the quasi-ion density at the edges builts up.[74,75] Thus, as temperature increases, the density of vacancies/trap states increases enhancing the nonradiative recombination rate, quenching the emission efficiency. It has been shown that longevity of planar perovskite solar cells/optical devices reduces drastically when temperature is increased from room temperature.[75] In our metasurface systems, we see an increase in temperature locally, which should definitely act as a catalyst in driving the materials toward lower longevity on exposure.

4. CONCLUSIONS

We have investigated the temperature- and power-dependent phonon behaviors in spatially patterned MAPbI thin films in order to determine the thermophysical properties of the MAPbI metasurfaces fabricated using the solution-mediated soft lithographic technique. We observe good replication of the patterned metasurfaces on the perovskite thin films using a home-made pressing machine at an applied pressure of 4 $kgcm^{-2}$, thus making the fabrication of metasurfaces on perovskite thin films realizable for nonspecialist research groups. We have demonstrated an enhanced absorption in the perovskite metasurface systems under solar illumination due to scattering and coupling to waveguide modes, which enhances the field inside the material. PL enhancement in the nanoholes is attributed to the combination of enhanced absorption, enhanced spontaneous emission, and enhanced photon outcoupling. A temperature-dependent PL measurement demonstrates the differential heat sensitivity of the perovskite metasurfaces with respect to the nontextured films. The use of a noncontact and simple tool in Raman spectroscopy allows us to study the local heating dynamics at the nanoscale level and investigate the thermal phonon behavior of perovskite thin films. Based on the Raman measurements, the first-order temperature coefficient of the phonon shifts has been determined for both pristine and patterned perovskite thin films. The increased phonon softening in nanohole perovskite thin films compared to the planar and striped samples is responsible for concentrating more heat locally and increasing the temperature. We are able to define, for the first time to our knowledge, a window of thermal sensitivity for MAPbI thin film−metasurface systems using which we can maximize device functionalities for solar cells and other optical applications. Based on our findings, we propose that selective nanopatterning of perovskite thin films can act as an innovative approach to develop localized thermal gradients for the fabrication of futuristic photothermal devices subject to further investigation.

■ ASSOCIATED CONTENT

Supporting Information

The Supporting Information is available free of charge at https://pubs.acs.org/doi/10.1021/acs.jpcc.0c10187.

Details of the soft lithographic method, XRD characterization of planar and imprinted films, core-level XPS spectra of MAPbI, optical microscopy and SEM images of imprinted thin films, deconvoluted Raman spectra of MAPbI, deconvoluted Raman spectra of MAPbI in the range of 80−200 cm^{-1} for different laser excitations,Raman shift as a function of temperature for 96 cm^{-1}

https://doi.org/10.1021/acs.jpcc.0c10187
J. Phys. Chem. C XXXX, XXX, XXX−XXX

vibrations for planar, striped, and nanohole thin films, and FDTD simulations (PDF)

AUTHOR INFORMATION

Corresponding Authors

Saswata Halder − *Department of Applied Physics, Faculty of Science and the Center for Nanoscience and Nanotechnology, The Hebrew University of Jerusalem, Jerusalem 9190401, Israel;* orcid.org/0000-0003-4079-5250; Email: saswata.halder@mail.huji.ac.il

Uriel Levy − *Department of Applied Physics, Faculty of Science and the Center for Nanoscience and Nanotechnology, The Hebrew University of Jerusalem, Jerusalem 9190401, Israel;* orcid.org/0000-0002-5918-1876; Email: ulevy@mail.huji.ac.il

Authors

Amit Kessel − *Department of Applied Physics, Faculty of Science and the Center for Nanoscience and Nanotechnology, The Hebrew University of Jerusalem, Jerusalem 9190401, Israel;* orcid.org/0000-0001-8113-100X

Noa Mazurski − *Department of Applied Physics, Faculty of Science and the Center for Nanoscience and Nanotechnology, The Hebrew University of Jerusalem, Jerusalem 9190401, Israel*

Complete contact information is available at: https://pubs.acs.org/10.1021/acs.jpcc.0c10187

Notes

The authors declare no competing financial interest.

ACKNOWLEDGMENTS

The authors acknowledge financial support from the Israeli Ministry of Science and Technology. The samples were fabricated, characterized, and measured at the Center for Nanoscience and Nanotechnology, the Hebrew University of Jerusalem.

REFERENCES

(1) Bi, D.; Tress, W.; Dar, M.-I.; Gao, P.; Luo, J.; Renevier, C.; Schenk, K.; Abate, A.; Giordano, F.; Correa Baena, J. P.; Decoppet, J. D.; Zakeeruddin, S. M.; Nazeeruddin, M. K.; Grätzel, M.; Hagfeldt, A. Efficient luminescent solar cells based on tailored mixed-cation perovskites. *Sci. Adv.* **2016**, *2*, No. e1501170.

(2) Liu, M.; Johnston, M. B.; Snaith, H. J. Efficient planar heterojunction perovskite solar cells by vapour deposition. *Nature* **2013**, *501*, 395−398.

(3) Chen, Z.; Turedi, B.; Alsalloum, A.-Y.; Yang, C.; Zheng, X.; Gereige, I.; AlSaggaf, A.; Mohammed, O. F.; Bakr, O.-M. Single-Crystal $MAPbI_3$ Perovskite Solar Cells Exceeding 21% Power Conversion Efficiency. *ACS Energy Lett.* **2019**, *4*, 1258−1259.

(4) Noh, J.-H.; Im, S.-H.; Heo, J.-H.; Mandal, T. N.; Seok, S.-I. Chemical Management for Colorful, Efficient, and Stable Inorganic−Organic Hybrid Nanostructured Solar Cells. *Nano Lett.* **2013**, *13*, 1764−1769.

(5) D'Innocenzo, V.; Srimath Kandada, A. R.; De Bastiani, M.; Gandini, M.; Petrozza, A. Tuning the Light Emission Properties by Band Gap Engineering in Hybrid Lead Halide Perovskite. *J. Am. Chem. Soc.* **2014**, *136*, 17730−17733.

(6) Mokkapati, S.; Catchpole, K. R. Nanophotonic light trapping in solar cells. *J. Appl. Phys.* **2012**, *112*, 101101.

(7) Cui, Y.; van Dam, D.; Mann, S. A.; van Hoof, N. J. J.; van Veldhoven, P. J.; Garnett, E. C.; Bakkers, E. P. A. M.; Haverkort, J. E. M. Boosting Solar Cell Photovoltage via Nanophotonic Engineering. *Nano Lett.* **2016**, *16*, 6467−6471.

(8) Mann, S. A.; Grote, R. R.; Osgood, R. M., Jr.; Alú, A.; Garnett, E. C. Opportunities and Limitations for Nanophotonic Structures To Exceed the Shockley−Queisser Limit. *ACS Nano* **2016**, *10*, 8620−8631.

(9) Jia, Y.; Kerner, R. A.; Grede, A. J.; Brigeman, A. N.; Rand, B. P.; Giebink, N. C. Diode-Pumped Organo-Lead Halide Perovskite Lasing in a Metal-Clad Distributed Feedback Resonator. *Nano Lett.* **2016**, *16*, 4624−4629.

(10) Whitworth, G. L.; Harwell, J. R.; Miller, D. N.; Hedley, G. J.; Zhang, W.; Snaith, H. J.; Turnbull, G. A.; Samuel, I. D. Nanoimprinted distributed feedback lasers of solution processed hybrid perovskites. *Opt. Express* **2016**, *24*, No. 23677.

(11) Brenner, P.; Stulz, M.; Kapp, D.; Abzieher, T.; Paetzold, U. W.; Quintilla, A.; Howard, I. A.; Kalt, H.; Lemmer, U. Highly stable solution processed metal-halide perovskite lasers on nanoim-printed distributed feedback structures. *Appl. Phys. Lett.* **2016**, *109*, 141106.

(12) Chen, S.; Roh, K.; Lee, J.; Chong, W. K.; Lu, Y.; Mathews, N.; Sum, T. C.; Nurmikko, A. A Photonic Crystal Laser from Solution Based Organo-Lead Iodide Perovskite Thin Films. *ACS Nano* **2016**, *10*, 3959−3967.

(13) Gholipour, B.; Adamo, G.; Cortecchia, D.; Krishnamoorthy, H. N. S.; Birowosuto, M. D.; Zheludev, N. I.; Soci, C. Organometallic Perovskite Metasurfaces. *Adv. Mater.* **2017**, *29*, No. 1604268.

(14) Wang, H.; Haroldson, R.; Balachandran, B.; Zakhidov, A.; Sohal, S.; Chan, J. Y.; Zakhidov, A.; Hu, W. Nanoimprinted Perovskite Nanograting Photodetector with Improved Efficiency. *ACS Nano* **2016**, *10*, 10921−10928.

(15) Cefarin, N.; Cian, A.; Sonato, A.; Sovernigo, E.; Suran, F.; Teklu, Z.; Zanut, A.; Pozzato, A.; Tormen, M. Nanostructuring methylammonium lead iodide perovskite by ultrafast nano imprinting lithography. *Microelectron. Eng.* **2017**, *176*, 106−110.

(16) Pourdavoud, N.; Wang, S.; Mayer, A.; Hu, T.; Chen, Y.; Marianovich, A.; Kowalsky, W.; Heiderhoff, R.; Scheer, H. C.; Riedl, T. Photonic Nanostructures Patterned by Thermal Nanoimprint Directly into Organo-Metal Halide Perovskites. *Adv. Mater.* **2017**, *29*, No. 1605003.

(17) Brittman, S.; Oener, S. Z.; Guo, K.; Āboliņš, H.; Koenderink, A. F.; Garnett, E. C. Controlling crystallization to imprint nanophotonic structures into halide perovskites using soft lithography. *J. Mater. Chem. C* **2017**, *5*, 8301−8307.

(18) Jeong, B.; Hwang, I.; Cho, S.-H.; Kim, E.-H.; Cha, S.; Lee, J.; Kang, H.-S.; Cho, S.-M.; Choi, H.; Park, C. Solvent-Assisted Gel Printing for Micropatterning Thin Organic−Inorganic Hybrid Perovskite Films. *ACS Nano* **2016**, *10*, 9026−9035.

(19) Liu, W.; Zhou, H.; Chen, G. Patterned Lead Halide Perovskite Crystals Fabricated by Microstructured Templates. *Cryst. Growth Des.* **2020**, *20*, 2803−2816.

(20) Verschuuren, M. A.; Knight, M. W.; Megens, M.; Polman, A. Nanoscale spatial limitations of large-area substrate conformal imprint lithography. *Nanotechnology* **2019**, *30*, 345301.

(21) Wang, H.; Liu, S. C.; Balachandran, B.; Moon, J.; Haroldson, R.; Li, Z.; Ishteev, A.; Gu, Q.; Zhou, W.; Zakhidov, A.; Hu, W. Nanoimprinted perovskite metasurface for enhanced photoluminescence. *Opt. Express* **2017**, *25*, No. A1162.

(22) Niu, G.; Li, W.; Meng, F.; Wang, L.; Dong, H.; Qiu, Y. Study on the stability of $CH_3NH_3PbI_3$ films and the effect of post-modification by aluminum oxide in all-solid-state hybrid solar cells. *J. Mater. Chem. A* **2014**, *2*, 705−710.

(23) Niu, G.; Guo, X.; Wang, L. Review of recent progress in chemical stability of perovskite solar cells. *J. Mater. Chem. A* **2015**, *3*, 8970−8980.

(24) Grätzel, M. The light and shade of perovskite solar cells. *Nat. Mater.* **2014**, *13*, 838−842.

(25) Li, X.; Tschumi, M.; Han, H.; Babkair, S. S.; Alzubaydi, R. A.; Ansari, A. A.; Habib, S. S.; Nazeeruddin, M. K.; Zakeeruddin, S. M.; Grätzel, M. Outdoor Performance and Stability under Elevated Temperatures and Long-Term Light Soaking of Triple-Layer Mesoporous Perovskite Photovoltaics. *Energy Technol.* **2015**, *3*, 551−555.

(26) Katan, C.; Mohite, A. D.; Even, J. Entropy in halide perovskites. *Nat. Mater.* **2018**, *17*, 377−379.
(27) Egger, D. A.; Bera, A.; Cahen, D.; Hodes, G.; Kirchartz, T.; Kronik, L.; Lovrincic, R.; Rappe, A. M.; Reichman, D. R.; Yaffe, O. What remains unexplained about the properties of halide perov-skites. *Adv. Mater.* **2018**, *30*, No. 1800691.
(28) Weller, M. T.; Weber, O. J.; Henry, P. F.; Di Pumpo, A. M.; Hansen, T. C. Complete structure and cation orientation in the perovskite photovoltaic methylammonium lead iodide between 100 and 352 K. *Chem. Commun.* **2015**, *51*, 4180−4183.
(29) Quarti, C.; Mosconi, E.; Ball, J. M.; D'Innocenzo, V.; Tao, C.; Pathak, S.; Snaith, H. J.; Petrozza, A.; de Angelis, F. Structural and optical properties of methylammonium lead iodide across the tetragonal to cubic phase transition: implications for perovskite solar cells. *Energy Environ. Sci.* **2016**, *9*, 155−163.
(30) Whitfield, P. S.; Herron, N.; Guise, W. E.; Page, K.; Cheng, Y. Q.; Milas, I.; Crawford, M. K. Structures, phase transitions and tricritical behaviour of the hybrid perovskite methyl ammonium lead iodide. *Sci. Rep.* **2016**, *6*, 35685.
(31) Comin, R.; Crawford, M. K.; Said, A. H.; Herron, N.; Guise, W. E.; Wang, X.; Whitfield, P. S.; Jain, A.; Gong, X.; McGaughey, A. J.; Sargent, E. H. Lattice dynamics and the nature of structural transitions in organolead halide perovskites. *Phys. Rev. B* **2016**, *94*, No. 094301.
(32) Liu, X.; Wu, X.; Ren, T. In situ and noncontact measurement of silicon membrane thermal conductivity. *Appl. Phys. Lett.* **2011**, *98*, 174104.
(33) Balandin, A. A.; Ghosh, S.; Bao, W.; Calizo, I.; Teweldebrhan, D.; Miao, F.; Lau, C. N. Superior thermal conductivity of single layer graphene. *Nano Lett.* **2008**, *8*, 902−907.
(34) Majumdar, D.; Biswas, S.; Ghoshal, T.; Holmes, J. D.; Singha, A. Probing Thermal Flux in Twinned Ge Nanowires through Raman Spectroscopy. *ACS Appl. Mater. Interfaces* **2015**, *7*, 24679−24685.
(35) Ben-Uliel, T.; Aviv, H.; Zhou, J.; Li, M.; Avadyayev, S.; Kapon, O.; Damle, V.; Yi, C.; Tischler, Y. Raman scattering obtained from laser excitation of $MAPbI_3$ single crystal. *Appl. Mater. Today* **2020**, *19*, No. 100571.
(36) Ledinský, M.; Löper, P.; Niesen, B.; Holovský, J.; Moon, S. J.; Yum, J. H.; De Wolf, S.; Fejfar, A.; Ballif, C. Raman Spectroscopy of Organic−Inorganic Halide Perovskites. *J. Phys. Chem. Lett.* **2015**, *6*, 401−406.
(37) Nakada, K.; Matsumoto, Y.; Shimoi, Y.; Yamada, K.; Furukawa, Y. Temperature-Dependent Evolution of Raman Spectra of Methylammonium Lead Halide Perovskites, $CH_3NH_3PbX_3$ (X = I, Br). *Molecules* **2019**, *24*, 626.
(38) Zhou, Y.; Garces, H. F.; Padture, N. P. Challenges in the ambient Raman spectroscopy characterization of methylammonium lead triiodide perovskite thin films. *Front. Optoelectron.* **2016**, *9*, 81−86.
(39) Xie, L. Q.; Zhang, T. Y.; Chen, L.; Guo, N.; Wang, Y.; Liu, G. K.; Wang, J. R.; Zhou, J. Z.; Yan, J. W.; Zhao, Y. X.; Mao, B. W.; Tian, Z. Q. Organic−inorganic interactions of single crystalline organolead halide perovskites studied by Raman spectroscopy. *Phys. Chem. Chem. Phys.* **2016**, *18*, 18112−18118.
(40) Pistor, P.; Ruiz, A.; Cabot, A.; Izquierdo-Roca, V. Advanced Raman Spectroscopy of Methylammonium Lead Iodide: Development of a Non-destructive Characterisation Methodology. *Sci. Rep.* **2016**, *6*, 35973.
(41) Segovia, R.; Qu, G.; Peng, M.; Sun, X.; Shi, H.; Gao, B. Evolution of Photoluminescence, Raman, and Structure of $CH_3NH_3PbI_3$ Perovskite Microwires Under Humidity Exposure. *Nanoscale Res. Lett.* **2018**, *13*, 79.
(42) Brivio, F.; Frost, J. M.; Skelton, J. M.; Jackson, A. J.; Weber, O. J.; Weller, M. T.; Goñi, A. R.; Leguy, A. M.; Barnes, P. R.; Walsh, A. Lattice dynamics and vibrational spectra of the orthorhombic, tetragonal, and cubic phases of methylammonium lead iodide. *Phys. Rev. B* **2015**, *92*, No. 144308.
(43) Ma, H.; Ma, Y.; Wang, H.; Slebodnick, C.; Alatas, A.; Urban, J. J.; Tian, Z. Experimental Phonon Dispersion and Lifetimes of Tetrago-nal $CH_3NH_3PbI_3$ Perovskite Crystals. *J. Phys. Chem. Lett.* **2019**, *10*, 1−6.
(44) Leguy, A. M. A.; Goñi, A. R.; Frost, J. M.; Skelton, J.; Brivio, F.; Rodríguez-Martínez, X.; Weber, O. J.; Pallipurath, A.; Alonso, M. I.; Campoy-Quiles, M.; Weller, M. T.; Nelson, J.; Walsh, A.; Barnes, P. R. F. Dynamic disorder, phonon lifetimes, and the assignment of modes to the vibrational spectra of methylammonium lead halide perovskites. *Phys. Chem. Chem. Phys.* **2016**, *18*, 27051−27066.
(45) Karakus, M.; Jensen, S. A.; D'Angelo, F.; Turchinovich, D.; Bonn, M.; Cánovas, E. Phonon-electron scattering limits free charge mobility in methylammonium lead iodide perovskites. *J. Phys. Chem. Lett.* **2015**, *6*, 4991−4996.
(46) Wright, A. D.; Verdi, C.; Milot, R. L.; Eperon, G. E.; Pérez-Osorio, M. A.; Snaith, H. J.; Giustino, F.; Johnston, M. B.; Herz, L. M. Electron-phonon coupling in hybrid lead halide perovskites. *Nat. Commun.* **2016**, *7*, 11755.
(47) Gold-Parker, A.; Gehring, P. M.; Skelton, J. M.; Smith, I. C.; Parshall, D.; Frost, J. M.; Karunadasa, H. I.; Walsh, A.; Toney, M. F. Acoustic phonon lifetimes limit thermal transport in methylammonium lead iodide. *Proc. Nat. Acad. Sci.* **2018**, *115*, 11905−11910.
(48) Pu, P.Y.; Cardona, M. *Fundamentals of Semiconductors: Physics and Materials Properties*, 4th Edition. Springer: Berlin, 2010.
(49) Kovalsky, A.; Wang, L.; Guo, X.; Dyck, J. S.; Burda, C. Temperature-Dependent Thermal Conductivity Study of $MAPbI_3$: Using Mild Aging To Reach a Thermal Percolation Threshold for Greatly Improved Heat Transport. *J. Phys. Chem. C* **2018**, *122*, 13243−13249.
(50) Hata, T.; Giorgi, G.; Yamashita, K. The Effects of the Organic-Inorganic Interactions on the Thermal Transport Properties of $CH_3NH_3PbI_3$. *Nano Lett.* **2016**, *16*, 2749−2753.
(51) Wang, M.; Lin, S. Anisotropic and ultralow phonon thermal transport in organic-inorganic hybrid perovskites: Atomistic insights into solar cell thermal management and thermoelectric energy conversion efficiency. *Adv. Funct. Mater.* **2016**, *26*, 5297−5306.
(52) Whalley, L. D.; Skelton, J. M.; Frost, J. M.; Walsh, A. Phonon anharmonicity, lifetimes and thermal transport in $CH_3NH_3PbI_3$ from many body perturbation theory. *Phys. Rev. B* **2016**, *94*, No. 220301.
(53) Beecher, A. N.; Semonin, O. E.; Skelton, J. M.; Frost, J. M.; Terban, M. W.; Zhai, H.; Alatas, A.; Owen, J. S.; Walsh, A.; Billinge, S. J. Direct observation of dynamic symmetry breaking above room temperature in methylammonium lead iodide perovskite. *ACS Energy Lett.* **2016**, *1*, 880−887.
(54) Li, B.; Kawakita, Y.; Liu, Y.; Wang, M.; Matsuura, M.; Shibata, K.; Ohira-Kawamura, S.; Yamada, T.; Lin, S.; Nakajima, K.; Liu, S. F. Polar rotor scattering as atomic level origin of low mobility and thermal conductivity of perovskite $CH_3NH_3PbI_3$. *Nat. Commun.* **2017**, *8*, 16086.
(55) Kessel, A.; Frydendahl, C.; Indukuri, S. R. K. C.; Mazurski, N.; Arora, P.; Levy, U. Soft Lithography for Manufacturing Scalable Perovskite Metasurfaces with Enhanced Emission and Absorption. *Adv. Opt. Mater.* **2020**, *8*, No. 2001627.
(56) Xiao, M.; Huang, F.; Huang, W.; Dkhissi, Y.; Zhu, Y.; Etheridge, J.; Gray-Weale, A.; Bach, U.; Cheng, Y. B.; Spiccia, L. A Fast Deposition-Crystallization Procedure for Highly Efficient Lead Iodide Perovskite Thin-Film Solar Cells. *Angew. Chem., Int. Ed.* **2014**, *53*, 9898−9903.
(57) Ball, J. M.; Stranks, S. D.; Hörantner, M. D.; Hüttner, S.; Zhang, W.; Crossland, E. J. W.; Ramirez, I.; Riede, M.; Johnston, M. B.; Friend, R. H.; Snaith, H. J. Optical properties and limiting photocurrent of thin-film perovskite solar cells. *Energy Environ. Sci.* **2015**, *8*, 602−609.
(58) Rocks, C.; Svrcek, V.; Maguire, P.; Mariotti, D. Understanding surface chemistry during $MAPbI_3$ spray deposition and its effect on photovoltaic performance. *J. Mater. Chem. C* **2017**, *5*, 902−916.
(59) Wang, J.; Cao, R.; Da, P.; Wang, Y.; Hu, T.; Wu, L.; Lu, J.; Shen, X.; Xu, F.; Zheng, G.; Chen, Z. Purcell effect in an organic-inorganic halide perovskite semiconductor microcavity system. *Appl. Phys. Lett.* **2016**, *108*, No. 022103.

https://doi.org/10.1021/acs.jpcc.0c10187
J. Phys. Chem. C XXXX, XXX, XXX−XXX

(60) Pelton, M. Modified Spontaneous Emission in Nanophotonic Structures. *Nat. Photonics* **2015**, *9*, 427−435.
(61) Richter, J. M.; Abdi-Jalebi, M.; Sadhanala, A.; Tabachnyk, M.; Rivett, J. P. H.; Pazos-Outón, L. M.; Gödel, K. C.; Price, M.; Deschler, F.; Friend, R. H. Enhancing photoluminescence yields in lead halide perovskites by photon recycling and light out-coupling. *Nat. Commun.* **2016**, *7*, 13941.
(62) Quarti, C.; Grancini, G.; Mosconi, E.; Bruno, P.; Ball, J. M.; Lee, M. M.; Snaith, H. J.; Petrozza, A.; De Angelis, F. The Raman Spectrum of the $CH_3NH_3PbI_3$ Hybrid Perovskite: Interplay of Theory and Experiment. *J. Phys. Chem. Lett.* **2014**, *5*, 279−284.
(63) Jalilian, R.; Sumanasekera, G. U.; Chandrasekharan, H.; Sunkara, M. K. Phonon Confinement and Laser Heating Effects in Germanium Nanowires. *Phys. Rev. B* **2006**, *74*, No. 155421.
(64) Liu, M. S.; Bursill, L. A.; Prawer, S.; Nugent, K. W.; Tong, Y. Z.; Zhang, G. Y. Temperature Dependence of Raman Scattering in Single Crystal GaN Films. *Appl. Phys. Lett.* **1999**, *74*, 3125−3127.
(65) Burke, H. H.; Herman, I. P. Temperature Dependence of Raman Scattering in $Ge_{1-x}Si_x$ Alloys. *Phys. Rev. B* **1993**, *48*, 15016−15024.
(66) Pisoni, A.; Jaćimović, J.; Barišić, O. S.; Spina, M.; Gaál, R.; Forró, L.; Horváth, E. Ultra-Low Thermal Conductivity in Organic-Inorganic Hybrid Perovskite $CH_3NH_3PbI_3$. *J. Phys. Chem. Lett.* **2014**, *5*, 2488−2492.
(67) He, Y.; Galli, G. Perovskites for Solar Thermoelectric Applications: A First Principle Study of $CH_3NH_3AI_3$ (A=Pb and Sn). *Chem. Mater.* **2014**, *26*, 5394−5400.
(68) Elbaz, G. A.; Ong, W.-L.; Doud, E. A.; Kim, P.; Paley, D. W.; Roy, X.; Malen, J. A. Phonon Speed, Not Scattering, Differentiates Thermal Transport in Lead Halide Perovskites. *Nano Lett.* **2017**, *17*, 5734−5739.
(69) Leguy, A. M. A.; Frost, J. M.; McMahon, A. P.; Sakai, V. G.; Kockelmann, W.; Law, C.; Li, X.; Foglia, F.; Walsh, A.; O'Regan, B. C.; Nelson, J.; Cabral, J. T.; Barnes, P. R. F. The dynamics of methylammonium ions in hybrid organic-inorganic perovskite solar cells. *Nat. Commun.* **2015**, *6*, 7780.
(70) Zhang, Z.; Zheng, W.; Wang, W.; Zhong, D.; Huang, F. Anisotropic temperature-dependence of optical phonons in layered PbI_2. *J. Raman. Spectrosc.* **2018**, *49*, 775−779.
(71) Shen, C.; Du, W.; Wu, Z.; Xing, J.; Ha, S.-T.; Shang, Q.; Xu, W.; Xiong, Q.; Liu, X.; Zhang, Q. Thermal conductivity of suspended single crystal $CH_3NH_3PbI_3$ platelets at room temperature. *Nanoscale* **2017**, *9*, 8281−8287.
(72) Sahoo, S.; Gaur, A. P. S.; Ahmadi, M.; Guinel, M. J. F.; Katiyar, R. S. Temperature-dependent Raman studies and thermal conductivity of few-layer MoS_2. *J. Phys. Chem. C* **2013**, *117*, 9042−9047.
(73) Schwenzer, J. A.; Rakocevic, L.; Gehlhaar, R.; Abzieher, T.; Gharibzadeh, S.; Moghadamzadeh, S.; Quintilla, A.; Richards, B. S.; Lemmer, U.; Paetzold, U. W. Temperature Variation-Induced Performance Decline of Perovskite Solar Cells. *ACS Appl. Mater. Interfaces* **2018**, *10*, 16390−16399.
(74) Shahivandi, H.; Vaezzadeh, M.; Saeidi, M. Theory of light-induced degradation in perovskite solar cells. *Sol. Energy Mater. Sol. Cells* **2020**, *208*, No. 110383.
(75) Shahivandi, H.; Vaezzadeh, M.; Saeidi, M. Study of the effect of temperature on light-induced degradation in Methylammonium lead iodine perovskite solar cells. *Sol. Energy Mater. Sol. Cells* **2020**, *218*, No. 110770.

https://doi.org/10.1021/acs.jpcc.0c10187
J. Phys. Chem. C XXXX, XXX, XXX−XXX